

Automated Estimation of Plasma Temperature and Density from Emission Spectroscopy

Todd A. Oliver*

Oden Institute for Computational Engineering and Sciences

University of Texas at Austin

Craig Michoski†

Sapientai LLC‡

Samuel Langendorf§ and Andrew LaJoie¶

Los Alamos National Laboratory

(Dated: December 21, 2023)

Abstract

This paper introduces a novel approach for automated estimation of plasma temperature and density using emission spectroscopy, integrating Bayesian inference with sophisticated physical models. We provide an in-depth examination of Bayesian methods applied to the complexities of plasma diagnostics, supported by a robust framework of physical and measurement models. Our methodology is validated through experimental observations, focusing on individual and sequential shot analyses. The results demonstrate the effectiveness of our approach in enhancing the accuracy and reliability of plasma parameter estimation, marking a significant advancement in the field of emission spectroscopy for plasma diagnostics. This study not only offers a new perspective in plasma analysis but also paves the way for further research and applications in nuclear instrumentation and related domains.

* oliver@oden.utexas.edu

† michoski@sapient-a-i.com

‡ Also at Oden Institute for Computational Engineering and Sciences, UT-Austin

§ samuel.langendorf@lanl.gov

¶ lajoiean@lanl.gov

I. INTRODUCTION

Spectroscopy is a powerful and versatile analytical tool that plays an increasingly critical role in a broad array of scientific and industrial fields. For example, atomic emission spectroscopy, centered on the study of emitted light spectra from excited atoms or molecules, offers a non-invasive and highly sensitive method for the characterization and identification of various substances. From environmental monitoring, medical diagnostics, and forensic analysis, to astrophysics, material science, and industrial process control, emission spectroscopy's extensive applications underscore its importance.

However, the quantities observed in emission spectroscopy—i.e., the intensities of light at different wavelengths—are generally not directly of interest in applications. Instead, it is common to extract the quantities of interest (QoI's) from these observables using a model. As an example, the simplest way to extract information from spectra is by assuming local thermodynamic equilibrium (LTE) conditions, and then leveraging the Boltzmann distribution law, where populations of distinct atomic energy levels are charted against their corresponding energies, yielding a graph whose slope bears a reciprocal relationship to the temperature of the system. Such plots are referred to as Boltzmann plots. However, in many application areas, such as in transient high energy laser plasma [1], the underlying LTE assumptions do not hold, and thus are generally considered inadequate for effectively interpreting the measured spectra. Thus, in order to accommodate for the added complexity present under non-LTE conditions (such as the presence of large local gradients), various complex kinetic models of the plasma have been developed and deployed, which effectively model the additional, e.g., radiative, transient, and diffusive processes present in these systems.

Thus, to extract information from the observed spectroscopic data, the data must be compared against model outputs to determine the conditions that generated the observations—i.e., the data processing takes the form of an inverse problem. Because both the observation and the models describing the physical process that generate it are complicated and include uncertainties that are difficult to quantify—due to noise and observational errors but also modeling approximations and assumptions—it is challenging to represent their effects upon the resulting inferred quantities of interest.

While it is well within the scope and capabilities of statistical and computational science

to provide solutions to this problem, the complexity and nuance of the problem itself alongside the significant laboratory challenge of simply getting experiments to function properly, can lead to a type of extreme instrumentalism [2] in laboratory environments where the spectra and models are, e.g., treated in potentially perilously reductive ways, such as by hasty and subjective visual inspection performed ‘over-the-bench’ by machine operators, to performing rudimentary (and potentially overly-simplistic) deterministic regression techniques, such as least squares residual analysis between the spectra and the kinetic model outputs. These interpretive conditions are then often reported with weakly justified generic absolute error bars in the literature, leading to a concern that the reported results are not rigorously and reliably understood by the operators themselves, or, for that matter, sufficiently aligned with reproducible scientific modes of inquiry and compliance.

In this work, we focus on solution methods to this problem that utilize Bayesian analysis [3] to provide principled and rigorous statistical methodologies, with the motivating factors being to develop and analyze a framework that allows for the automation of uncertainty quantification in this specific context. A broad overview of how Bayesian spectral fitting methods have been developed and implemented for spectroscopic data analysis can be found in [4, 5], and more specifically the utilization of these types of models for evaluating emission spectra in plasma discharges in [6] and fusion devices [7–10]. Similar approaches can be found for gamma-ray spectroscopy [11], Nuclear Magnetic Resonance spectroscopy [12, 13], transmission spectroscopy [14, 15], diffuse reflectance spectroscopy [16], and quantum noise spectroscopy [17]. Finally, mixture models are considered in [18], while automation techniques for these types of techniques are addressed in [19].

The specific motivating experiment for this work is the Plasma Liner Experiment (PLX) at Los Alamos National Laboratory, and particularly, the collection of emission spectra from the formed spherical plasma liners. Emission spectroscopy is a powerful diagnostic technique for the PLX liner plasmas, which are comprised largely of mid-density $10^{15} - 10^{17}$ cm^{-3} low temperature $1 - 5$ eV plasmas with typically argon species. The plasma emits a rich series of lines in the visible spectrum, which are readily collected via fiber-coupled spectrometers and digitized on CCD detectors, accumulating a large volume of data in the form of images. Comparison of the emission lines to atomic physics models contains useful information on the liner electron temperature and ionization state evolution, but to date this comparison has been performed manually, by generation of a large number

of comparison plots between observation and many candidate model spectra, and manual comparison to determine estimates of the plasma parameters. This procedure has limited the amount of information that can be gleaned from the spectra and left them somewhat under-utilized on many experimental campaigns, motivating the development of a more powerful and automated method.

The structure of this paper is organized as follows. Section II describes the inference approach developed by integrating Bayesian inference techniques with base physical models. Section III discusses the details of the experimental system under consideration, and Section IV shows the results of the application of the Bayesian inference approach to the experimental data interpretation on this experimental system. Finally, we provide a conclusion and future directions in Section V.

II. INFERENCE APPROACH

To determine the state of the plasma—including, potentially, the temperature, density, and composition—a model relating these variables to the observed spectral data is required. The plasma properties of interest are then inferred based on what parameter values lead to agreement between the modeled and observed spectra. This process—i.e., determining the value that minimizes the misfit between the experiment and the model—naturally takes the form of an optimization problem, but a straightforward optimization does not automatically account for uncertainty, which is introduced both by uncertainties inherent in any measurement process as well as by approximations inherent in any modeling process. To account for these uncertainties, a Bayesian inference approach is adopted here. In this approach, the solution of the inverse problem is a probability distribution for the plasma properties of interest. This probability distribution characterizes not only the most likely values of the parameters but also the relative probability of other values, accounting for the uncertainties in the measurements and models underlying the analysis.

A. Bayesian Inference Overview

To be concrete, let θ denote the collection of plasma properties we hope to infer. Further, let y_{obs} denote the observations, and let \mathcal{M} denote a physical model that maps the parameters

θ to the observations y_{obs} . Given such a model, the approach here is to infer the values of the parameters by finding those values that make the output from the model best match the observations. If both the model and the observations were perfect—i.e., free from errors and uncertainties—then there would exist values of the parameters, denoted θ^* , such that

$$y_{obs} = \mathcal{M}(\theta^*),$$

and we could discover such parameter values by solving the following minimization problem:

$$\theta^* = \arg \min_{\theta} \|y_{obs} - \mathcal{M}(\theta)\|,$$

where $\|y_{obs} - \mathcal{M}(\theta)\|$ denotes a metric function (usually a norm) measuring the discrepancy between the observations and the model.

Of course, in practice, it is almost never the case that both the observations y_{obs} and model \mathcal{M} are entirely free from errors and uncertainties. In this situation, if only the “best” parameter values are of interest, then the optimization approach is still feasible. However, it is often of interest to find not only the best fit but all values that lead to adequate, in some sense, agreement between the measurements and the model and to characterize the relative plausibility of these values. When such uncertainties are of interest, the Bayesian statistical framework provides a coherent and self-consistent methodology for such analysis.

Bayesian methods have become common in a wide range of scientific applications involving inference problems [3, 20–25]. In the Bayesian framework, the solution of the inference problem is given by the probability density for the parameters of interest θ conditioned on the observations y_{obs} —an object known as the “posterior” probability density. Denoting this posterior by $\pi(\theta|y)$, Bayes’ theorem states that

$$\pi(\theta|y) = \frac{\pi(\theta) \pi(y|\theta)}{\pi(y)},$$

where $\pi(\theta)$ is known as the “prior” and $\pi(y|\theta)$ is the “likelihood”. The denominator $\pi(y)$ is a normalizing constant that ensures that the posterior integrates to one and will not be discussed further here. The prior characterizes any information about the parameters that is available independent from the observations y_{obs} . For this work, the prior is taken to be a uniform distribution over a set of possible plasma conditions selected by the analyst. To complete the formulation, the likelihood must be specified. The likelihood is based on two models: 1) the physical model \mathcal{M} , which is described in section §II B and 2) a probabilistic model representing all relevant uncertainties, which is described in section §II C.

B. Physical Models

For the sake of exposition, the physical model under consideration here is split into two components: 1) the *base physics model*, which determines the expected spectrum under given conditions, not accounting for measurement imperfections, and 2) the *measurement model*, which determines the expected observed spectrum under given conditions and outputs of the base physics model, and does account for potential measurement distortions.

1. Base physics model

Detailed modeling of emission spectra from plasmas is a broad and deep subject, and several modeling paradigms can be (and have been) applied depending on the plasma conditions of interest. One paradigmatic categorization is whether the plasma can be described by certain equilibria, such as local-thermal-equilibrium (LTE) conditions [26], which hold in dense plasmas when the plasma collisions are frequent and fully govern electron energy state populations, and coronal-equilibrium conditions [27], which hold in rarefied plasmas where the dominant de-excitation of electrons is radiative relaxation to the ground state. In contrast, at intermediate densities, the modeling paradigm of interest generally used to model the relative contributions of these mechanisms is a collisional-radiative (CR) model, which solves for the populations of electron energy states at given conditions and thus the relative strength of emission lines [28].

The simplest version of these models describe local (zero dimensional) light emission from a point source at a given plasma condition, but additional physical effects may occur en route to the observational instrument, such as those caused by optical opacity of the plasma, etc. These effects can be treated by techniques common in radiation transport, including, for example, radiation diffusion and characteristics methods, which can be solved simultaneously to determine the electron energy level populations. For the plasma conditions of interest in this paper, the plasma density is low enough that it can be assumed to be optically thin for the visible emission lines of interest, and effects of radiation transport can subsequently be neglected.

A complication for the analysis of spectra of optically thin plasmas to experimental measurements is that most practical experimental light collection schemes lead to the collection

of light from a finite volume of the plasma, typically a narrow line-of-sight captured by a viewing lens or collimated-fiber-optic that delivers light from the plasma to a spectrometer. Thus, the recorded spectrum contains contributions from different spatial regions of the plasma, which may in general correspond to different physical (local) densities, temperatures, etc. As a consequence, a simplifying modeling assumption is made along the spatial profile of the discrete plasma conditions that assumes QoI homogeneity along the spectrometer’s line of sight, thus allowing for the inverse problem to be solved over the entire line-integrated volume of plasma observed. While it is possible to enrich this simplifying assumption by either modifying the underlying model (and hence usually its modeling assumptions) or by adding additional experimental diagnostics, the resulting problem is still more than likely to remain largely under-determined [29].

In this paper the atomic spectra are obtained using the CR model PrismSPECT [30]. PrismSPECT is a non-local (or local) thermodynamic equilibrium collisional-radiative model that calculates emission and absorption spectrum assuming a uniform plasma given a fixed electron temperature T_e and density ρ [31, 32]. The Bayesian inference model utilized by SpectAI is independent of the underlying model generating the spectra that are being compared. Thus, in principle, these inputs can be obtained using any atomic emission and absorption spectra model. For example, other collisional radiative based models that could, in principle, be used include FLYCHK [33, 34], ATOMIC [35], ABAKO [36], OPAL [37], OPAS [38], SCO-RCG [39], etc., or see [40] for a broad overview and comparison of available codes/models.

2. *Measurement model*

The *measurement model* utilizes the *base physics model* while accounting for two additional separate issues. First, the instrument model introduces spectral broadening present beyond the physical broadening mechanisms represented in the base physics model, the instrument being limited in spectral resolution for example depending on the groove density of its diffraction grating. Second, the measurement model accounts for the data conversion between what the spectrometer records intensity in (i.e. as a function of pixel index), and the corresponding wavelength used for interpreting the corresponding base physical model output. In principle, other effects could be treated, but we restrict to these two in the

present work.

These measurement features are essentially characteristics of the observation equipment—i.e., the spectrometer and any associated infrastructure. Thus, in principle, they can be determined by an instrument calibration process to a known calibration source, which is commonly done. With a good calibration, one can then assume that these features are simply fixed for the Bayesian analysis described in §II C, which we do here. However, since even small mismatches between the observed and modeled spectra can significantly affect the inference results, mismatches that could occur for example from a slight rotation of the diffraction grating in the positioning system, we have found it beneficial to include a method to estimate these features using the observations of interest, rather than using separate calibration data. These techniques are described below.

a. Instrument line broadening The effect of instrument broadening is represented by convolving a Gaussian function with the output of the model from section §II B 1. Specifically, given the output of the base physics model, $\mathcal{M}_b(\lambda; \theta)$, the model predicts that the spectrum that should be observed when accounting for instrument broadening is given by

$$\mathcal{M}(\lambda; \theta, \sigma) = \int_{-\infty}^{\infty} \mathcal{M}_b(\tilde{\lambda}; \theta) g(\lambda - \tilde{\lambda}; \sigma) d\tilde{\lambda}, \quad (1)$$

where

$$g(s; \sigma) = \frac{1}{\sqrt{2\pi\sigma^2}} \exp\left(-\frac{1}{2} \frac{s^2}{\sigma^2}\right), \quad (2)$$

and the parameter σ is the standard deviation, which determines the broadening width.

b. Pixel to wavelength mapping The intensity measurement is recorded as a function of pixel index. In order to compare this to the model $\mathcal{M}(\lambda; \theta)$, the pixel index p must be mapped to the corresponding wavelength. This is provided by a generic function $\lambda(p)$, where the function $\lambda(p)$ is estimated from measurements recorded for a known source. Thus, this map is typically provided independent of the measurements of interest. In this work, we use a linear mapping:

$$\lambda(p) = mp + b, \quad (3)$$

where the parameters m and b may be set by the analyst. However, it has been observed that even small deviations in the parameters m and b , or small modeling errors that lead to shifts in the modeled spectrum, can contaminate the inference process and lead to temperature inferences that are implausible. To avoid this problem, the parameters m and b can also be

calibrated using the observed spectrum and the modeled spectrum at a selected condition. As with σ , this calibration could be incorporated into the Bayesian inference, but this complication is beyond the scope of the present work. Instead, the parameters m and b are determined using a deterministic least-squares solve using peak locations from a chosen experiment and single simulation. That is, given the highest N intensity peaks at locations λ_k , $k = 1, \dots, N$ in the selected simulation and the corresponding N highest peaks at pixels p_k , $k = 1, \dots, N$ in the observed spectrum, m and b are given by

$$(m, b) = \arg \min_{\hat{m}, \hat{b}} \sum_{k=1}^N \left(\lambda_k - \hat{m} p_k - \hat{b} \right)^2, \quad (4)$$

where the peaks are ordered according to increasing wavelength in the simulation and increasing pixel in the observations. This aligns the peaks in the selected simulation with those in the experiment as well as possible given the linear fit. Example results for this inference are shown in Fig. 4

C. Probabilistic Model

The resulting likelihood from the Bayesian procedure encodes the plausibility of the observation for given values of the parameters, accounting for uncertainties in both the observations and the model. Thus, to formulate a likelihood, we require a probabilistic model of the discrepancy between the model and the observation. Such a model could be the source of nearly endless development and debate. Here, we adopt a practical approach that does not require detailed information about sources of error in either the observation or the physical model. As such, it is applicable in situations where the details of the precise sources of error are not well-understood, as is common in practice with complex experiments and models. However, the approach does account for known characteristics of data produced by emission spectroscopy. Specifically, we assume that both the observations and the model predictions consist of a set of strong “lines” embedded in a background signal. An example of such an observation is shown in Figure 7. The likelihood model used here is based upon a simple algebraic model of functions that have such features.

The algebraic spectrum model takes the following form:

$$\mathcal{I}(\lambda) = \sum_{i=1}^N s_i g(\lambda; \lambda_i, w_i) + b(\lambda), \quad (5)$$

where \mathcal{I} is the spectral intensity, λ is the wavelength, N is the number of lines, s_i is the strength of the i th line, g is a line shape function, λ_i is the location of the i th line, w_i is the width of the i th line, and b is the background. For the remainder of this work, we assume that the background is negligible or can be exactly removed prior to the analysis, and thus it will be neglected going forward.

In designing a likelihood model, the task is to assign probabilities to observed differences. Toward this end, consider the difference between two spectra. Using superscripts to distinguish between these two spectra and assuming (5) is appropriate for both, their difference can be written as

$$\delta\mathcal{I}(\lambda) = \mathcal{I}^{(1)}(\lambda) - \mathcal{I}^{(0)}(\lambda) = \sum_{i=1}^{N_1} s_i^{(1)} g^{(1)}(\lambda; \lambda_i^{(1)}, w_i^{(1)}) - \sum_{i=1}^{N_0} s_i^{(0)} g^{(0)}(\lambda; \lambda_i^{(0)}, w_i^{(0)}).$$

Spectra that are “close” will have the same number of lines, $N_1 = N_0 = N$, and be described using the same line shape functions $g^{(1)} = g^{(0)} = g$. In this case,

$$\delta\mathcal{I}(\lambda) = \sum_{i=1}^N s_i^{(1)} g(\lambda; \lambda_i^{(1)}, w_i^{(1)}) - s_i^{(0)} g(\lambda; \lambda_i^{(0)}, w_i^{(0)})$$

Finally, we can further simplify by linearizing this result—i.e., by writing spectrum (1) as a Taylor series expansion around spectrum (0) parameters and dropping all terms higher than first order. Specifically,

$$\begin{aligned} \delta\mathcal{I}(\lambda) &= \sum_{i=1}^N (s_i^{(0)} + \delta s_i) (g(\lambda; \lambda_i^{(0)} + \delta\lambda_i, w_i^{(0)} + \delta w_i) - s_i^{(0)} g(\lambda; \lambda_i^{(0)}, w_i^{(0)})) \\ &\approx \sum_{i=1}^N \delta s_i g(\lambda; \lambda_i, w_i) + s_i \frac{\partial g}{\partial \lambda_i} \delta\lambda_i + s_i \frac{\partial g}{\partial w_i} \delta w_i, \end{aligned}$$

where $\delta s_i = s_i^{(1)} - s_i^{(0)}$, $\delta\lambda_i = \lambda_i^{(1)} - \lambda_i^{(0)}$, $\delta w_i = w_i^{(1)} - w_i^{(0)}$.

This development serves as the basis for the probabilistic model of the discrepancy between the observed and modeled spectra. Specifically, the model that follows is given by:

$$\mathcal{I}_{obs}(\lambda) - \mathcal{M}(\lambda; \theta) = \sum_{i=1}^N \delta s_i g(\lambda; \lambda_i, w_i) + s_i \frac{\partial g}{\partial \lambda_i} \delta\lambda_i + s_i \frac{\partial g}{\partial w_i} \delta w_i + \epsilon \quad (6)$$

where

$$\delta s_i \sim N(0, \eta^2), \quad \delta\lambda_i \sim N(0, \ell^2), \quad \delta w_i \sim N(0, \sigma^2),$$

and ϵ is a zero-mean white noise Gaussian process. Clearly this model has a number of parameters: N ; s_i , λ_i , and w_i for $i = 1, \dots, N$; η , ℓ , σ , and β . Determination of these hyperparameters is described below. Once these values are fixed, the probabilistic model is entirely defined by the distributions for δs_i , $\delta \lambda_i$, δw_i and δb , which are Gaussian, the form (6), which is linear in these parameters, and the additive Gaussian noise ϵ . Thus, the resulting probabilistic model of the discrepancy and the resulting likelihood is a Gaussian process (GP).

D. Hyperparameters

The parameters of the likelihood model, i.e., the hyperparameters, can be split into two qualitatively different groups. The first group includes N , s_i , λ_i , and w_i . These parameters characterize the original spectrum that the likelihood model is describing deviations from. As such, these parameters are identified based on the original observation. We use standard, “off-the-shelf” techniques to determine these parameters. Specifically, we use the `find_peaks` function from the `scipy.signal` package [41], that utilizes standard peak prominence heuristics to determine peak locations. To avoid spurious peaks due to noise in the observations, peaks are required to have a height that is at least 0.03 times the maximum intensity in the observation window, and peaks are required to have a prominence of 0.01 times the maximum intensity in the observation window.

The second group of parameters includes η , ℓ , σ , and β . These parameters control how the stochastic model assigns probability around the result of the deterministic model. These parameters are determined in a preprocessing step that occurs prior to the Bayesian inference. First, reasonable values of the physical model parameters are estimated using standard least-squares minimization. Then, denoting these initial parameter values by θ^* , the misfit ϵ^* is computed via $\epsilon^* = \mathcal{I}_{obs} - \mathcal{M}(\theta^*)$. Given this misfit, the parameters δs_i , $\delta \lambda_i$, δw_i , and δb can be determined by solving a linear least-squares problem to minimize the discrepancy between the misfit model (6) and the computed ϵ^* . Specifically, we solve the following optimization problem

$$\delta s_i^*, \delta \lambda_i^*, \delta w_i^* = \arg \min_{\delta s_i, \delta \lambda_i, \delta w_i} \|\epsilon^* - e(\delta s_i, \delta \lambda_i, \delta w_i)\|, \quad (7)$$

where

$$e(\delta s_i, \delta \lambda_i, \delta w_i) = \sum_{i=1}^N \delta s_i g(\lambda; \lambda_i, w_i) + s_i \frac{\partial g}{\partial \lambda_i} \delta \lambda_i + s_i \frac{\partial g}{\partial w_i} \delta w_i. \quad (8)$$

This leads to N (the number of lines) values for each parameter. Then, the standard deviation parameters η , ℓ , and σ are determined by taking the observed standard deviation of this best fit over all the lines.

E. Summary

To summarize the overall approach, the solution of the inverse problem is given by the posterior probability distribution for the plasma density and temperature, ρ and T , given the observed intensity, I :

$$\pi(\rho, T|I) \propto \pi(\rho, T) \pi(I|\rho, T),$$

where the prior $\pi(\rho, T)$ is uniform over a range of conditions and the likelihood $\pi(I|\rho, T)$ which incorporates the physical, measurement, and probabilistic models described in § II B–§ II D. Since the prior is taken to be uniform here, the posterior is proportional to the likelihood function. The likelihood model is Gaussian in the intensity, but, because the forward model relating the density and temperature to the intensity is nonlinear, the resulting posterior probability over density and temperature is not necessarily Gaussian and cannot be sampled easily. While specialized algorithms are available for exploring such distributions, such as various Markov chain Monte Carlo (MCMC) methods [42], these algorithms require the evaluation of the forward model inside the sampling loop. Since the forward model evaluation is the most computationally expensive component of this approach, and since the space of interest is only two-dimensional, we choose a grid-based approach instead. In this approach, the model is run on a grid in density, temperature space *a priori* and then the posterior is evaluated on that same grid. In this way, a single set of simulations can be used to support the inference for a large number of experimental observations, which effectively amortizes the computational effort over the entire experimental campaign and dramatically reduces the time required for the inference on any single experiment. Thus, given an observed spectrum, the steps to evaluate this posterior probability are as follows:

1. Run a set of physical model simulations—here using PrismSpect, as described in Section II B—to compute the predicted spectrum for a set of plausible ρ_i, T_i conditions,

assuming the gas composition is known.

2. Determine the measurement model hyperparameters (see Section II B 2), including:
 - The line broadening parameter, σ , and
 - The pixel to wavelength mapping parameters, m and b .
3. Determine the probabilistic model hyperparameters, as discussed in Section II D.
4. Evaluate the posterior at points where the simulations were run, $\pi(\rho_i, T_i|I)$, by evaluating the likelihood given the simulation results and observations, as described in Section II C.

As discussed previously, step 1 need only be performed once for a given set of experiments at similar conditions.

III. EXPERIMENTAL OBSERVATIONS

The inference framework described above is applied to the analysis of results from a series of experiments at PLX. In these experiments, two unmagnetized argon plasma jets are collided head-on at varied (relative fixed) velocity and density, to study the collisionality of the supersonic plasmas under these conditions. The plasma behavior under these conditions is relevant to the prospects of PLX / PJMIF as a spherical compression driver, specifically as related to occurrence of collisional plasma shocks vs. kinetic interpenetration of the jets. These phenomena have been observed in previous studies on PLX. Emission spectroscopy is collected from these experiments, and is an important diagnostic in the overall experiment for constraining the plasma electron temperature and average ionization state \bar{Z} .

Figure 1 shows a diagram of the experimental setup and spectroscopic diagnostic layout. Light is collected from the central volume of the colliding plasma jets and imaged onto the entrance slit of a Chromex 500is imaging spectrometer, which is coupled to a PCO Dicam Pro intensified CCD camera. The spatial direction resolved by the spectrometer is aligned with the jet collision axis, and it was envisioned that this would provide spatially resolved data across plasma shocks when they occurred. In implementation, spatial resolution was significantly blurred by effects of perspective distortion in the entrance optics viewing the transparent plasma, so effective spatial resolution was not obtained. The data therefore

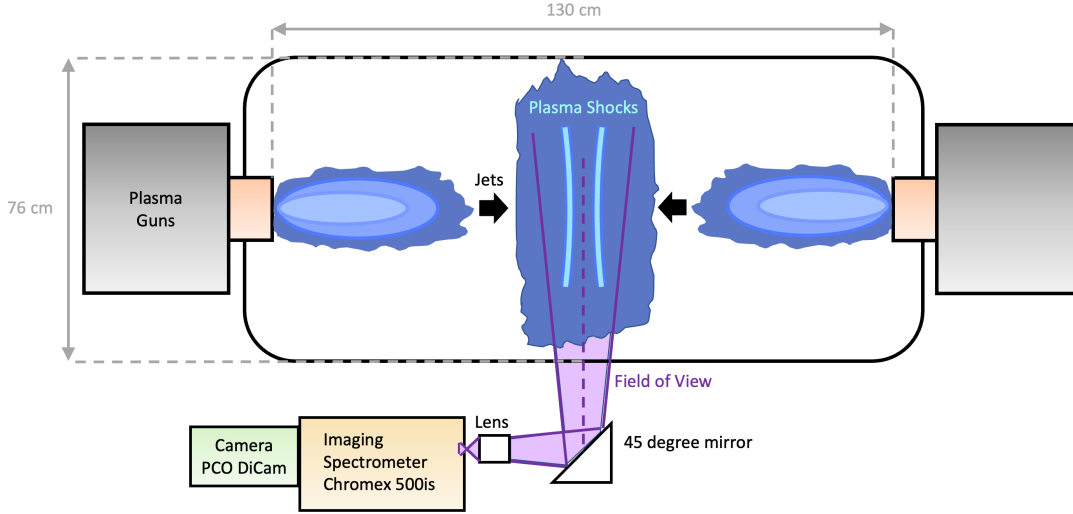


FIG. 1: A diagram of the experimental setup of the jet merging chamber that uses plasma guns from PLX. The purple highlighted region indicates the spectrometer field of view.

Shot numbers	P inlet (psig)	V (kV)	avg. jet velocity (km/s)
7328-7365	50	4	16 ± 1.7
7366-7398, 7497-7504	30	4.5	28 ± 4.1
7399-7433	40	4.25	26 ± 5.6
7434-7470	45	4.25	23 ± 3.7
7471-7496	35	4.25	27 ± 5.9
7505-7540	20	4.5	52 ± 1.5

TABLE I: Experimental shot settings, and average measured plasma jet velocity

constitute a spatially-integrated measure over the plasma volume. Data are temporally resolved by control of the camera exposure time and delay, acquiring one frame of data per shot. Shots are repeated with varied camera delays to build up a time-resolved evolution of the emission spectrum at each jet operating condition.

A series of shots are performed spanning different jet operating conditions, summarized in Table I. The main experimental settings that are varied are the charge voltage of the plasma gun capacitor bank, and the inlet pressure to the gas puff valve. With higher bank

voltage, more accelerating current is delivered, resulting in a higher velocity. With higher inlet pressure, more gas is injected into the gun, resulting in a heavier jet and ultimately a slower velocity.

Figure 2 shows raw data obtained from an experimental shot, and the same data processed compared to a PrismSPECT simulated spectrum. Strong lines of singly-ionized argon are consistently observed across many experimental operating conditions, with relatively subtle changes in the spectrum from shot to shot. This is expected, as the radiative cooling from the ionized argon increases significantly with temperature in this range ~ 2 eV, and acts to clamp the temperature from rising greatly above this level. A colder liner temperature is typically desirable in PLX / PJMIF to keep liner sound speed and density expansion low, and to increase the liner Mach number. This dataset is analyzed using the developed inference approach.

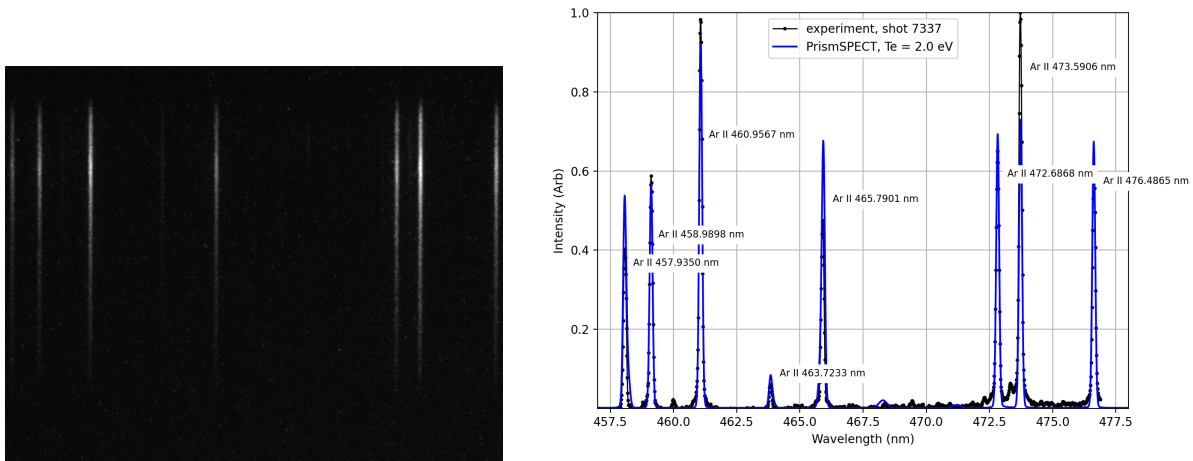


FIG. 2: (a) Raw data image from shot 7337. (b) Processed and binned data from shot 7337, overlaid with PrismSPECT simulated spectrum. Visible strong lines of singly-ionized argon labeled.

IV. RESULTS

The analysis can be decomposed into two phases: (1) a pre-processing phase, where the line broadening and pixel to wavelength map parameters (§II B) and probabilistic model

hyperparameters (§IID) are determined, and (2) the Bayesian inference phase. Sample results from each phase are presented for cases identified in Table I.

A. Pre-processing Phase Results

To determine the pixel to wavelength mapping, the least-squares problem defined in (4) is solved. The data for this problem is determined using standard peak finding techniques[43]. Figure 3 shows example results from the peak finding phase for solving the

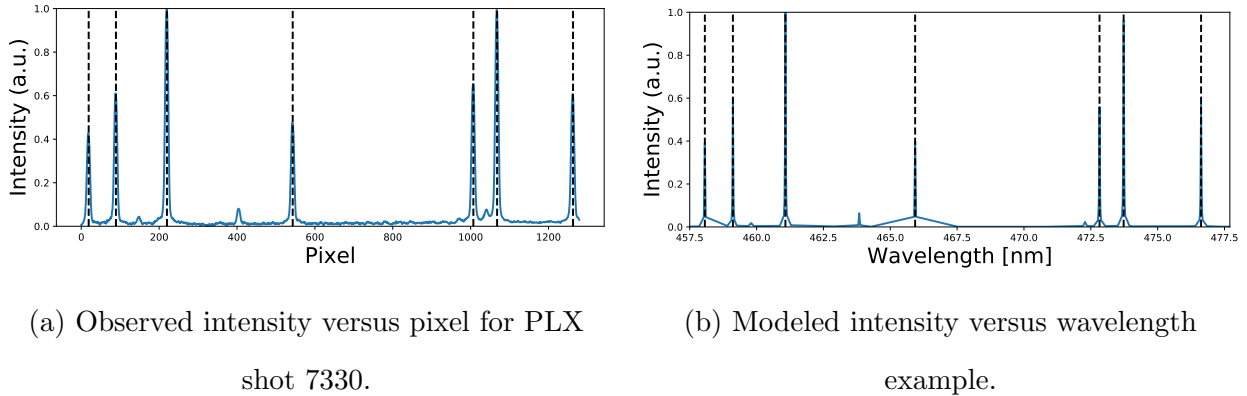


FIG. 3: Intensity versus pixel and wavelength with peaks indicated by the vertical dashed lines.

resulting least-squares problem gives the pixel with wavelength mapping shown in Figure 4. The fit succeeds for this case and there is no suggestion that a richer parameterization of the mapping is necessary.

B. Bayesian Inference Results

The inference results are split into two sections. First, to give a sample of the full picture of information that is obtained, joint posteriors for density and temperature for individual shots are shown. The features observed in the posterior as well as the fits between the PrismSpect predictions and the measured spectra are examined. Second, we use the results to look for trends in the measured temperature as a function of the experimental settings. These results reinforce the importance of accounting for uncertainty in the analysis of such measurements.

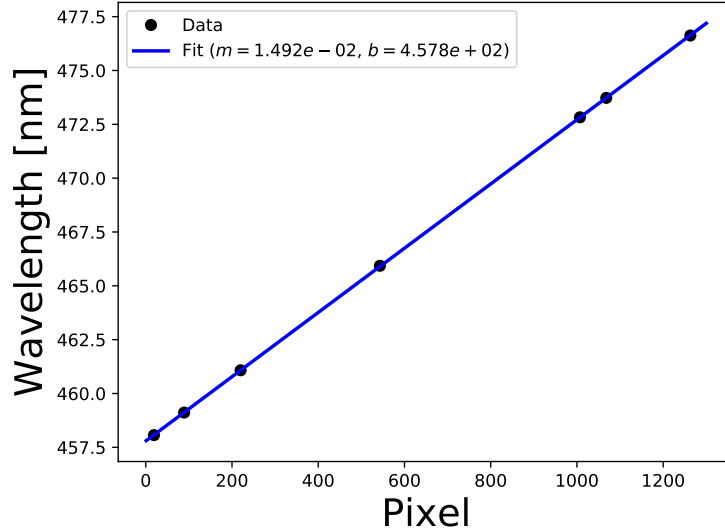


FIG. 4: Pixel to wavelength mapping determined by fitting peak wavelengths as a linear function of peak pixels.

1. Individual shot results

Figure 5 shows the joint posterior probability for six shots taken on October 1, 2021. These shots—specifically, 7330, 7331, 7337, 7338, 7343, and 7344—are all at the same nominal conditions of 50 psig inlet pressure for the gas puff valve and 4 kV voltage of the plasma gun capacitor bank. The spectra are measured at different camera delay times, with 7330 and 7331 using a delay of $58 \mu\text{s}$ while 7337 and 7338 have a $52 \mu\text{s}$ delay and 7343 and 7344 have a $46 \mu\text{s}$ delay. Dependencies on camera delay time and other parameters are examined more closely in Section IV B 2. Here, these shots are used as representative individual spectra, and the results show some notable features. First, the uncertainty is not negligible. The range of non-negligible posterior probability generally spreads over an interval of approximately 0.5 eV. Second, the posterior probability does not always concentrate around a single peak. The results from shots 7337 and 7338 show this clearly. Since the Bayesian approach provides a full probability distribution as the solution of the inverse problem, such behavior is allowed when multiple conditions fit the data similarly well, even if they are separated in parameter space.

To get a better sense of the inferred temperature, since this is often the primary quantity of interest of such measurements, the joint posterior is marginalized over the density to give

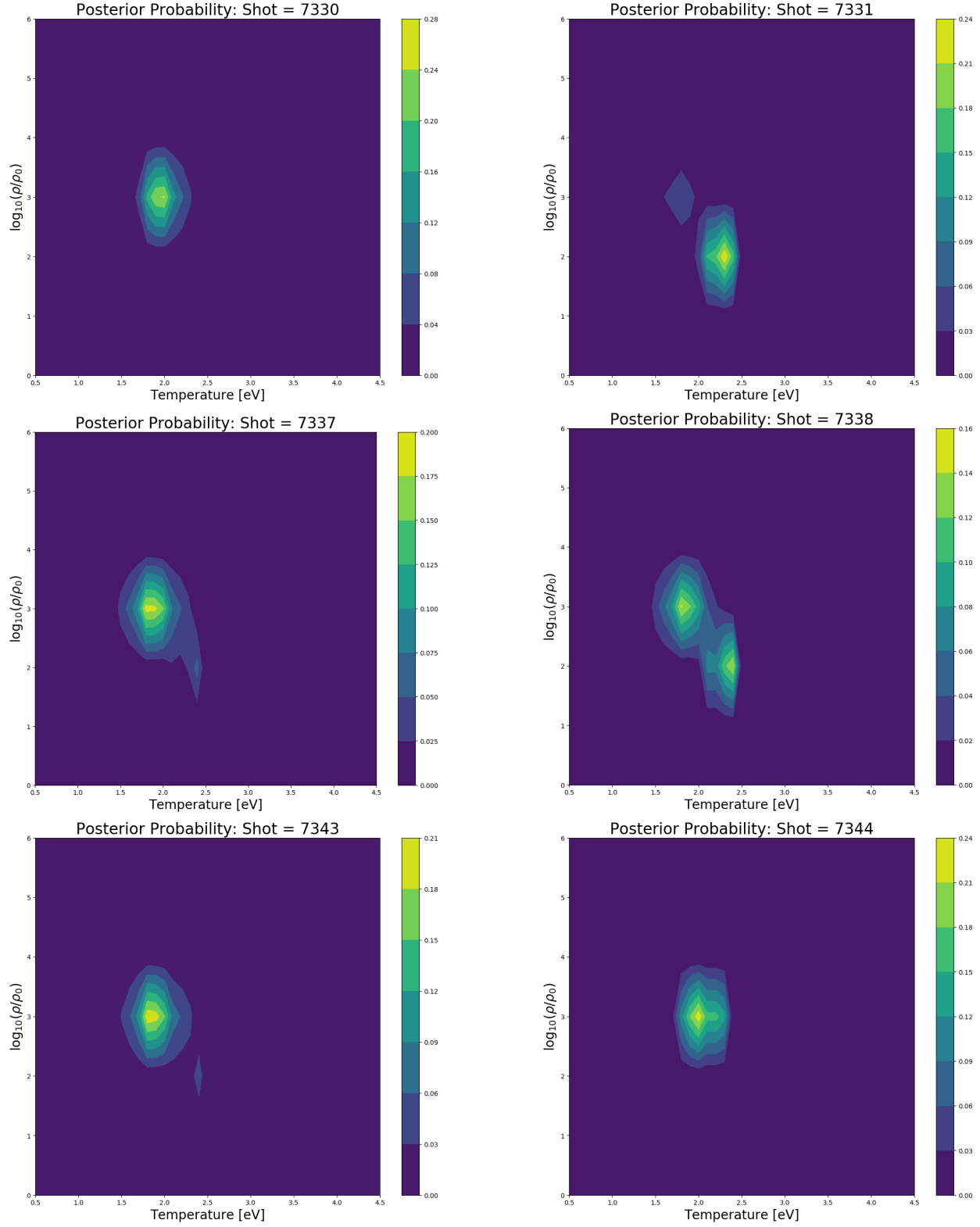


FIG. 5: Joint posterior probability distributions for temperature and density inferred from spectra recorded during six PLX shots on 10/1/2021.

the marginal posterior distribution for the temperature alone; specifically,

$$\pi(T|I) = \int \pi(\rho, T|I) d\rho.$$

Figure 6 shows these marginal distributions for the same shots as in Figure 5. Again, the marginal probability results demonstrate that the uncertainties are significant. Qualitatively speaking, these result from the fact that model results at multiple conditions provide similar fits to the measured spectrum. Figure 7 demonstrates this fact using shot 7330 as an example. The figure shows that over the range of highly probable conditions, as determined by the inference process, the spectrum is qualitatively very similar. Thus, given the inherent measurement precision and modeling errors, it is difficult to determine the conditions more precisely given the available information.

2. Shot sequence results

In addition to examining individual shots, the spectra obtained at different conditions can be analyzed in an attempt to identify the dependency of the state of the plasma upon various experimentally controllable parameters. As an example, Figure 8 shows the dependence of the inferred temperature on the camera delay time, which corresponds to the time in the evolution of the plasma formed in the core of the merging jets, for the different inlet pressure and capacitor bank voltages shown in Table I. The results show that, with the present measurements and models, it is very difficult to identify any meaningful trends, because the uncertainty is large enough that it is unclear whether changes in the most probable temperature between conditions are real. To evaluate the uncertainty estimates, we note that the data set includes some conditions that are repeated. These repeats lead to a scatter in the results at the same delay times shown in the figure, but all the repeats fall within the uncertainty of each other. This gives some confidence that the uncertain estimates from the inference are not too small. Further, the scatter between repeats is roughly of the same magnitude as the uncertainty, indicating that our uncertainty estimates are not dramatically too large. Thus, we are forced to conclude that any trends in the temperature are swamped by the uncertainty and cannot be determined from these measurements alone.

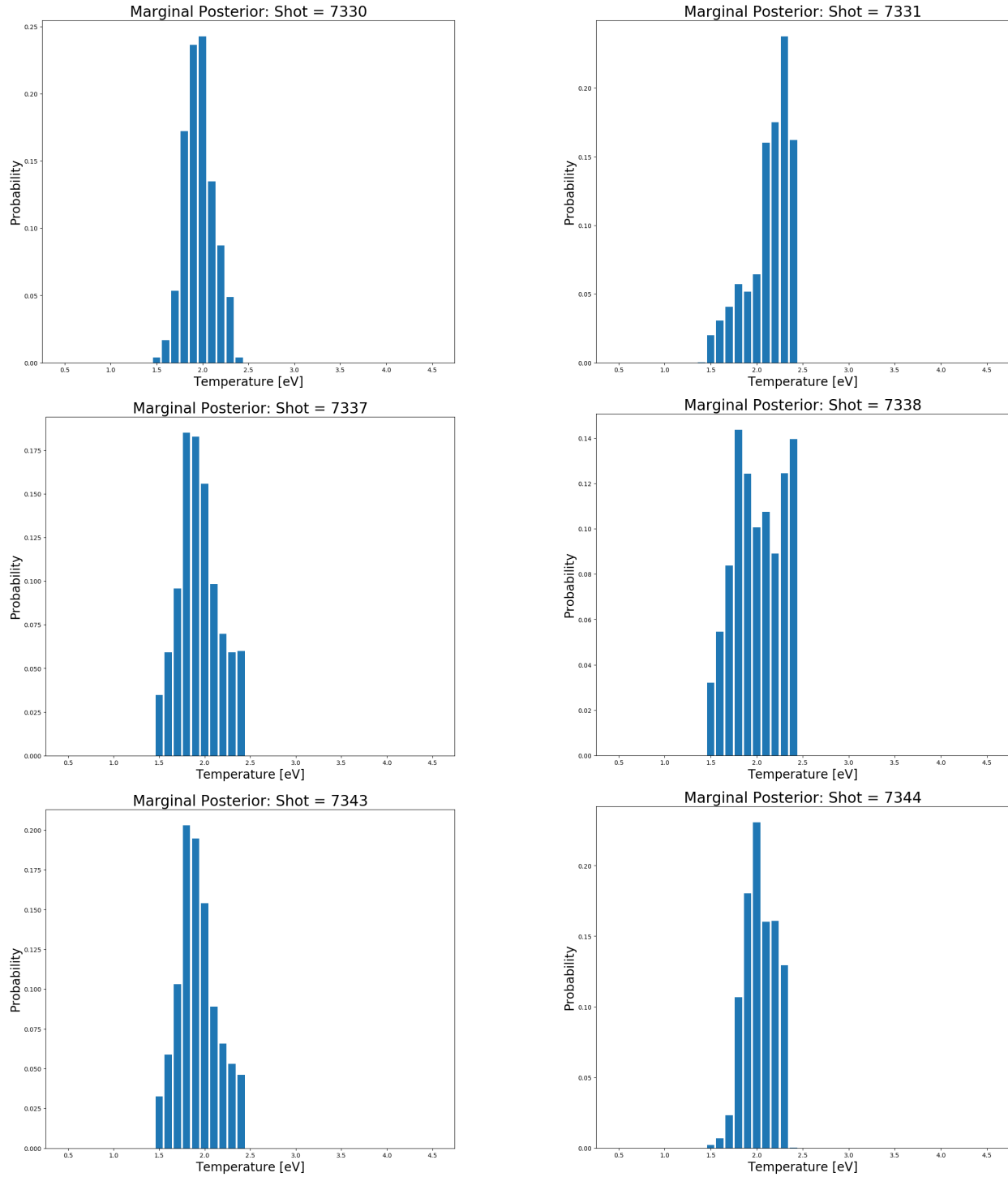


FIG. 6: Marginal posterior probability distributions for temperature inferred from spectra recorded during six PLX shots on 10/1/2021.

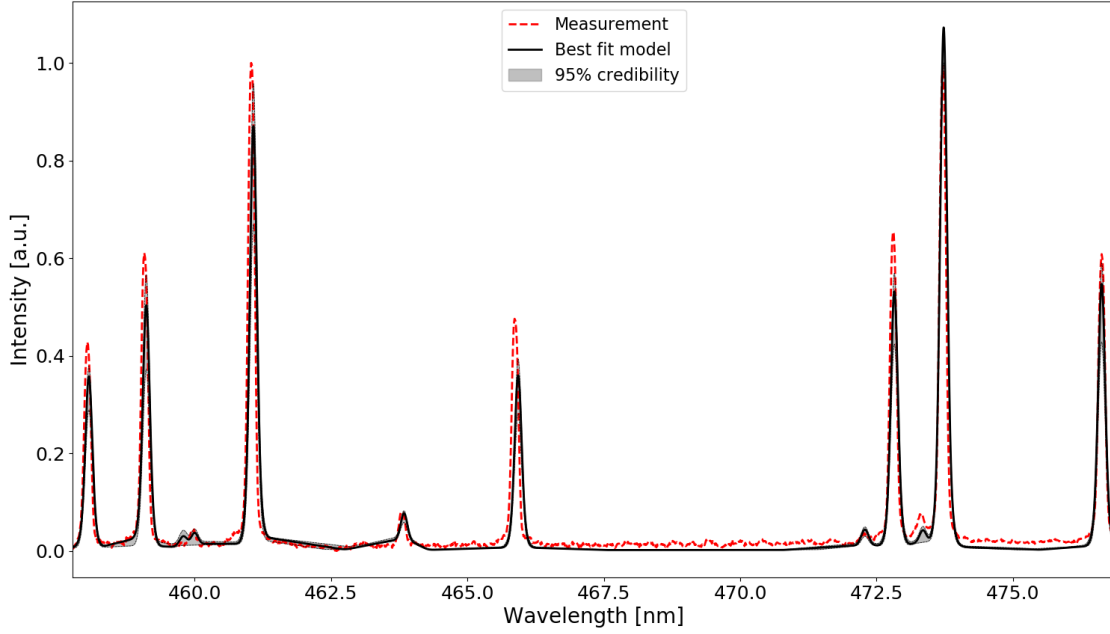


FIG. 7: Comparison of the measured and modeled spectrum for shot 7330.

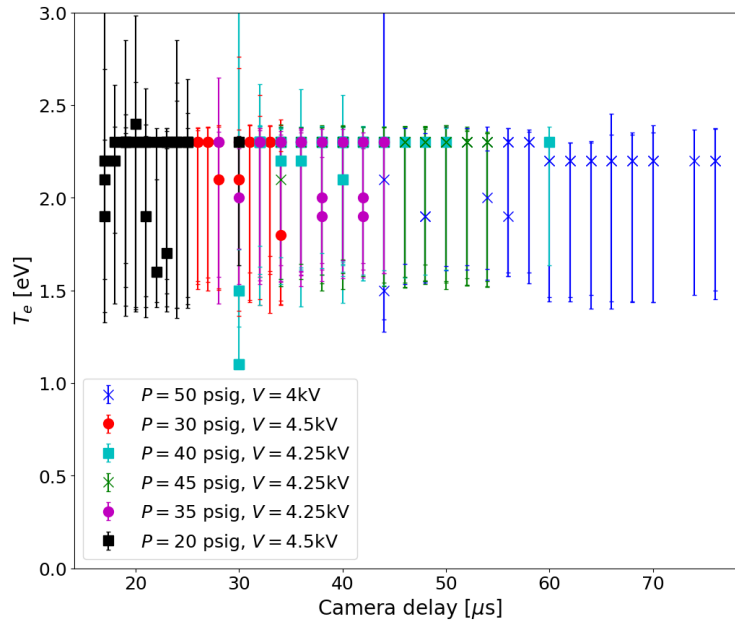


FIG. 8: Inferred temperature as a function of camera delay time for various inlet pressures and capacitor bank volrages. The symbols indicate the maximum a posteriori temperature and the uncertainty bar indicates the 95% credibility interval for T_e . Some conditions are repeated, leading to different results at the same nominal conditions.

V. CONCLUSIONS

In this study, we have presented an approach for the automated estimation of plasma temperature and density from emission spectroscopy, integrating physical and probabilistic models by way of Bayesian inference. The robustness of our approach lies in its ability to assimilate complex physical models with probabilistic reasoning, offering a nuanced understanding of plasma characteristics. The detailed overview of Bayesian inference, coupled with the foundational physical models, set the stage for a methodological framework that is both rigorous and adaptable.

Our experimental results on a series of experiments at PLX have yielded promising results and consist of a pre-processing phase and a Bayesian inference phase. The results from this inference, particularly the individual shot and shot sequence analyses, have demonstrated the efficacy of our approach in providing accurate and reliable estimations of plasma parameters. These results underscore the potential of Bayesian methods in the field of plasma diagnostics, often offering a significant leap over traditional estimation techniques.

The current state of the technique offers many paths for possible extensions and improvements. First, for practical reasons, the inferences of some parameters—e.g., the hyperparameters of the probabilistic model—are conducted separately from the primary inference for the plasma properties. These inferences could be unified, allowing the effects of calibration uncertainties to be included and quantified. Second, the process could be extended to enable inference for trace species, enabling the identification of contaminants. More broadly, there is significant potential for adoption of these techniques in plasma research and other related fields. For instance, the ability to accurately estimate plasma temperature and density is not only critical for understanding plasma behavior but also pivotal for advancing nuclear instrumentation and its applications.

In conclusion, this study contributes a novel and effective tool for the field of plasma diagnostics, harnessing the power of Bayesian inference and sophisticated physical modeling. It opens up new avenues for research and application, promising to enhance the precision and understanding of plasma processes, as well as finding application in other areas of experimental analysis, such as analytical chemistry, etc. Future work will focus on refining the models further and exploring the integration of additional data sources, to extend the capabilities and applicability of the methodology.

VI. ACKNOWLEDGEMENTS

This work was partially supported by U.S. ARPA-E Award No. DE-AR0001265. This manuscript has been authored in collaboration with Los Alamos National Laboratory/Triad National Security, LLC, Contract No. 89233218CNA000001, with the U.S. Department of Energy/National Nuclear Security Administration. The views and opinions of authors expressed herein do not necessarily state or reflect those of the United States Government or any agency thereof.

- [1] G. Cristoforetti, E. Tognoni, and L. Gizzi, *Spectrochimica Acta Part B: Atomic Spectroscopy* **90**, 1 (2013).
- [2] J. Leplin, *A Companion to the Philosophy of Science*, 393 (2017).
- [3] U. Von Toussaint, *Reviews of Modern Physics* **83**, 943 (2011).
- [4] N. M. Cao and F. Sciortino, *IEEE Transactions on Plasma Science* **48**, 22 (2019).
- [5] S. G. Razul, W. Fitzgerald, and C. Andrieu, *Nuclear Instruments and Methods in Physics Research Section A: Accelerators, Spectrometers, Detectors and Associated Equipment* **497**, 492 (2003).
- [6] D. Dodt, A. Dinklage, R. Fischer, and D. Loffhagen, in *AIP Conference Proceedings*, Vol. 872 (American Institute of Physics, 2006) pp. 264–271.
- [7] R. Fischer, C. Fuchs, B. Kurzan, W. Suttrop, E. Wolfrum, and A. U. Team, *Fusion science and technology* **58**, 675 (2010).
- [8] S. A. Bozhenkov, M. Beurskens, A. Dal Molin, G. Fuchert, E. Pasch, M. Stoneking, M. Hirsch, U. Höfel, J. Knauer, J. Svensson, *et al.*, *Journal of Instrumentation* **12**, P10004 (2017).
- [9] G. Verdoolaege, M. Von Hellermann, R. Jaspers, M. Ichir, and G. Van Oost, in *AIP Conference Proceedings*, Vol. 872 (American Institute of Physics, 2006) pp. 541–548.
- [10] F. Sciortino, N. Howard, E. Marmor, T. Odstreil, N. Cao, R. Dux, A. Hubbard, J. Hughes, J. Irby, Y. Marzouk, *et al.*, *Nuclear Fusion* **60**, 126014 (2020).
- [11] T. Burr, A. Favalli, M. Lombardi, and J. Stinnett, *Algorithms* **13**, 265 (2020).
- [12] D. V. Rubtsov and J. L. Griffin, *Journal of Magnetic Resonance* **188**, 367 (2007).

- [13] Y. Matviychuk, E. von Harbou, and D. J. Holland, *Journal of Magnetic Resonance* **285**, 86 (2017).
- [14] W. Pluriel, J. Leconte, V. Parmentier, T. Zingales, A. Falco, F. Selsis, and P. Bordé, *Astronomy and Astrophysics-A&A* **658**, A42 (2022).
- [15] T. Zingales, A. Falco, W. Pluriel, and J. Leconte, *Astronomy & Astrophysics* **667**, A13 (2022).
- [16] M. Hohmann, A. Karabayir, P. Herzler, M. Späth, F. Klämpfl, and M. Schmidt, *Journal of Biophotonics* **14**, e202100205 (2021).
- [17] C. Ferrie, C. Granade, G. Paz-Silva, and H. M. Wiseman, *New Journal of Physics* **20**, 123005 (2018).
- [18] H.-S. Park, S.-W. Yoo, and C.-H. Jun, *The Korean Journal of Applied Statistics* **22**, 759 (2009).
- [19] W. Li, Z. Chijian^o, and F. Yuan, in *Information Computing And Automation (In 3 Volumes)-Proceedings Of The International Conference* (World Scientific, 2008) p. 328.
- [20] R. P. Christian, *The Bayesian Choice* (Springer, 2001).
- [21] E. T. Jaynes, *Probability theory: The logic of science* (Cambridge university press, 2003).
- [22] J. Kaipio and E. Somersalo, *Statistical and Computational Inverse Problems* (Springer, 2005).
- [23] D. Calvetti and E. Somersalo, *Introduction to Bayesian Scientific Computing* (Springer, 2007).
- [24] S. H. Cheung, T. A. Oliver, E. E. Prudencio, S. Prudhomme, and R. D. Moser, *Reliability Engineering & System Safety* **96**, 1137 (2011).
- [25] T. A. Oliver, G. Terejanu, C. S. Simmons, and R. D. Moser, *Computer Methods in Applied Mechanics and Engineering* **283**, 1310 (2015).
- [26] T. Fujimoto and R. McWhirter, *Physical Review A* **42**, 6588 (1990).
- [27] T. Fujimoto, *Journal of the Physical Society of Japan* **34**, 216 (1973).
- [28] Y. Ralchenko, *Modern methods in collisional-radiative modeling of plasmas* (Springer, 2016).
- [29] I. Craig and J. Brown, *Astronomy and Astrophysics*, vol. 49, no. 2, June 1976, p. 239-250. Research supported by the Science Research Council. **49**, 239 (1976).
- [30] J. MacFarlane, I. Golovkin, P. Woodruff, D. Welch, B. Oliver, T. Mehlhorn, and R. Campbell, in *Proc. Inertial Fusion and Sciences Applications*, Vol. 457 (2003).
- [31] H. Sawada, *Experimental investigation of a direct-drive shock wave heated and compressed planar target relevant to ICF* (University of Rochester, 2008).

- [32] B. Han, F. Wang, D. Salzmann, and G. Zhao, Publications of the Astronomical Society of Japan **67** (2015).
- [33] H.-K. Chung, W. Morgan, and R. Lee, Journal of Quantitative Spectroscopy and Radiative Transfer **81**, 107 (2003).
- [34] H.-K. Chung, M. Chen, W. Morgan, Y. Ralchenko, and R. Lee, High energy density physics **1**, 3 (2005).
- [35] P. Hakel, M. Sherrill, S. Mazevet, J. Abdallah Jr, J. Colgan, D. Kilcrease, N. Magee, C. Fontes, and H. Zhang, Journal of Quantitative Spectroscopy and Radiative Transfer **99**, 265 (2006).
- [36] R. Florido, R. Rodríguez, J. Gil, J. Rubiano, P. Martel, E. Mínguez, and R. Mancini, Physical Review E **80**, 056402 (2009).
- [37] C. Iglesias and F. Rogers, The Astrophysical Journal **371**, 408 (1991).
- [38] G. Mondet, C. Blancard, P. Cossé, and G. Faussurier, The Astrophysical Journal Supplement Series **220**, 2 (2015).
- [39] T. Nagayama, J. Bailey, R. Mancini, C. Iglesias, S. Hansen, C. Blancard, H. Chung, J. Colgan, P. Cosse, G. Faussurier, *et al.*, High Energy Density Physics **20**, 17 (2016).
- [40] R. Piron, F. Gilleron, Y. Aglitskiy, H.-K. Chung, C. J. Fontes, S. B. Hansen, O. Marchuk, H. A. Scott, E. Stambulchik, and Y. Ralchenko, High Energy Density Physics **23**, 38 (2017).
- [41] P. Virtanen, R. Gommers, T. E. Oliphant, M. Haberland, T. Reddy, D. Cournapeau, E. Burovski, P. Peterson, W. Weckesser, J. Bright, *et al.*, Nature methods **17**, 261 (2020).
- [42] L. Martino, Digital Signal Processing **75**, 134 (2018).
- [43] Specifically, we use the `find_peaks` function from the `scipy.signal` package. See https://docs.scipy.org/doc/scipy/reference/generated/scipy.signal.find\protect_peaks.html.